SCIENTIFIC REPORTS

OPEN

SUBJECT AREAS:
TOPOLOGICAL INSULATORS
NANOSCALE DEVICES

Received
26 February 2014

Accepted
10 April 2014

Published
7 May 2014

Correspondence and requests for materials should be addressed to J.T. (tian5@purdue.edu) or Y.P.C. (yongchen@purdue.edu)

# Quantum and Classical Magnetoresistance in Ambipolar Topological Insulator Transistors with Gate-tunable Bulk and Surface Conduction

Jifa Tian[1,2], Cuizu Chang[3,4], Helin Cao[1,2], Ke He[3], Xucun Ma[3], Qikun Xue[4] & Yong P. Chen[1,2,5]

[1]Department of Physics and Astronomy, Purdue University, West Lafayette, Indiana 47907, USA, [2]Birck Nanotechnology Center, Purdue University, West Lafayette, Indiana 47907, USA, [3]Beijing National Laboratory for Condensed Matter Physics, Institute of Physics, Chinese Academy of Sciences, Beijing 100190, P. R. China, [4]State Key Laboratory for Low-Dimensional Quantum Physics, Department of Physics, Tsinghua University, Beijing 100084, P. R. China, [5]School of Electrical and Computer Engineering, Purdue University, West Lafayette, Indiana 47907, USA.

**Weak antilocalization (WAL) and linear magnetoresistance (LMR) are two most commonly observed magnetoresistance (MR) phenomena in topological insulators (TIs) and often attributed to the Dirac topological surface states (TSS). However, ambiguities exist because these phenomena could also come from bulk states (often carrying significant conduction in many TIs) and are observable even in non-TI materials. Here, we demonstrate back-gated ambipolar TI field-effect transistors in $(Bi_{0.04}Sb_{0.96})_2Te_3$ thin films grown by molecular beam epitaxy on $SrTiO_3(111)$, exhibiting a large carrier density tunability (by nearly 2 orders of magnitude) and a metal-insulator transition in the bulk (allowing switching off the bulk conduction). Tuning the Fermi level from bulk band to TSS strongly enhances both the WAL (increasing the number of quantum coherent channels from one to peak around two) and LMR (increasing its slope by up to 10 times). The SS-enhanced LMR is accompanied by a strongly nonlinear Hall effect, suggesting important roles of charge inhomogeneity (and a related classical LMR), although existing models of LMR cannot capture all aspects of our data. Our systematic gate and temperature dependent magnetotransport studies provide deeper insights into the nature of both MR phenomena and reveal differences between bulk and TSS transport in TI related materials.**

Topological insulators (TIs) are an exotic state of quantum matter with nominally-insulating bulk and spin-momentum-locked Dirac fermion conducting surface states, promising potential applications in both nanoelectronics and spintronics[1–3]. Many interesting phenomena based on such topological surface states (TSS) have been proposed, such as Majorana fermions[4,5], exciton condensation[6], topological magnetoelectric effect[7], etc. $Bi_2Se_3$, $Bi_2Te_3$, and $Sb_2Te_3$ have been proposed and identified as prototype 3D TIs, possessing TSS with a linear dispersion of energy vs momentum in the bulk band gap (BBG)[8–11] However, most of these commonly studied TI materials inevitably have impurities or defects during their growth, resulting in a doped bulk which can account for a significant part of the conductance, making it difficult to study and utilize the novel electronic transport of the TSS. To access the surface transport properties of the 3D TIs, various strategies have been attempted to suppress the bulk conduction, for example by (compensation) doping, increasing the surface-to-volume ratio, or electric gating. A ternary compound $(Bi_{1-x}Sb_x)_2Te_3$, an alloyed mixture of $Bi_2Te_3$ and $Sb_2Te_3$, has been shown as a promising group of 3D TIs with excellent tunability of the electronic properties by varying the composition $x$[12,13]. Recently, the quantum anomalous Hall effect[14] has been successfully observed in Cr doped $(Bi_xSb_{1-x})_2Te_3$, adding further interests to examine the underlying electronic transport properties of this ternary TI system.

Most transport studies of TIs have focused on magnetotransport[15], particularly magnetoresistance (MR). In a few experiments, Shubnikov–de Haas oscillations[11,16–18] with $\pi$ Berry phase were observed and used as direct

transport evidence for TSS Dirac fermions. However, the majority of TIs do not show such quantum oscillations because of disorder or inhomogeneity. Instead two other MR features have been commonly used in a large number of experiments to probe the transport signature of TSS: the weak antilocalization (WAL) at low magnetic ($B$) field[19–29] and linear MR (LMR)[30–34] at high $B$. However, given the parallel conducting surface and bulk channels often existing in TIs, ambiguities can arise when attributing WAL and LMR to TSS, as both phenomena could also arise from bulk states, and have even been observed in many non-TI-based spin-orbit-coupled or narrow-gap semiconductors[35,36]. For example, it is often difficult to exactly determine the roles of TSS in earlier WAL studies in TIs with metallic bulk conduction, where the reported WAL from only one coherent channel likely reflects the strongly mixed contributions from bulk and surfaces coupled together[19,24–27]. More recent experiments utilizing gate tuning of the surface-bulk coupling and the number of phase coherent channels in $Bi_2Se_3$ thin films[21,22] have pointed out a possibility to extract the transport signatures of the TSS through careful analysis. Despite these progresses, most experiments so far still dealt with significant bulk conduction, and did not reach or clearly demonstrate the so-called "topological transport" regime, where bulk is truly insulating and surface dominates the conduction. In addition to the ambiguities associated with WAL, the nature of LMR[13,30–34,36–41] itself has also been debated (with both classical[38,39] and quantum models[40,41]) since its observation in silver chalcogenides and other narrow gap semiconductors[36,37]. The recent observations of LMR in TIs[30–34] have been often interpreted in the framework of the quantum LMR[30,32] due to the gapless energy spectrum of TSS, although it is not fully clear if the quantum model[40,41] applies without a clean separation of bulk and TSS. A better understanding of the nature of LMR will benefit its many proposed applications in areas such as spintronics or magnetoelectric sensors[32].

In this work, we perform a systematic transport study of $(Bi_{0.04}Sb_{0.96})_2Te_3$ TI thin films (10 nm) grown by molecular beam epitaxy (MBE) on $SrTiO_3$ (STO)(111) substrates (250 μm, Figs. 1a,b). Using STO (with its very high relative dielectric constant $\varepsilon_r$ at low temperature) as a back gate, we demonstrate a large tunability of the carrier density ($n$, by nearly 2 orders of magnitude) and Fermi level ($E_f$) in our film, exhibiting an ambipolar field-effect (FE). This allows us to realize a gate-tuned metal-to-insulator transition in the bulk of our sample, thus tuning the transport from the bulk-dominated regime (where the $E_f$ is in the bulk valence band, BVB) to the topological transport regime (where $E_f$ is in the TSS) with surface-dominated conduction at low temperature. We also systematically map out the gate and temperature dependent WAL and LMR (along with Hall measurements), revealing differences between the bulk and TSS transport regimes and providing more insights on the nature of such MR phenomena.

## Results

**Bulk metal-insulator transition and ambipolar field effect.** The temperature dependence of the zero $B$ field longitudinal resistance ($R_{xx}$ vs $T$) measured at different gate voltages $V_g$ are presented in Fig. 1c. The STO substrate, with its very high $\varepsilon_r$ at low $T$[13,42], gives a strong gate modulation to the sample's $n$. By increasing $V_g$, $E_f$ can be tuned from the BVB to BBG (intercepting TSS, insets of Fig. 1c). For $V_g = -60$ V, where $E_f$ is in the BVB, the corresponding $R_{xx}$ decreases with decreasing $T$ and saturates at low $T$, demonstrating a characteristic metallic bulk conduction. The temperature below which $R_{xx}$ appears to saturate moves to a smaller value at $V_g = -10$ V, suggesting weakened metallic behavior. Further increasing $V_g$ to $-5$ V, $R_{xx}$ shows a clear upturn below ~30 K, indicating the appearance of an insulting behavior (attributed to freezing-out of thermally excited bulk carriers) in the film. Such a bulk insulating behavior can be significantly enhanced by further lifting $E_f$ into the BBG ($V_g = 0$ V) and eventually, for $V_g > 10$ V the bulk insulating behavior onsets at a $T$ as high as ~100 K, with $R_{xx}$ approximately saturating with very weak $T$-dependence for $T < 30$ K. The bulk insulating behavior observed in $V_g = 0$ V is consistent with the ARPES observation of $E_f$ located in the BBG in as-grown films[12]. The nearly saturated $R_{xx}$ (terminating the insulating behavior) for $V_g > 10$ V indicates a remnant conduction that can be attributed to the TSS in the BBG[11,16–18,43,44] dominating the charge transport at low $T$ (see Fig. S1). Our observations demonstrate a striking transition from the metallic to insulating behavior in the bulk of such films, driven by $E_f$ (tuned by $V_g$). This transition can also be regarded as that from a "topological metal" to a "topological insulator", and is foundational to our study to clarify the relative roles played by the bulk and TSS in MR features.

Fig. 1d shows the FE behavior measured at $B = 0$ T and $T = 1.4$ K. All the curves of $R_{xx}$ vs $V_g$ show ambipolar FE. For example, $R_{xx}$ of curve "1" is weakly modulated by the gate as $V_g < -20$ V, but increases significantly and reaches a peak of ~12 kΩ when $V_g$ is increased to ~12 V (the charge neutral point (CNP), $V_{CNP}$, showing an on-off ratio of 600%) before decreasing again upon further increasing $V_g$. Furthermore, an appreciable hysteresis in $R_{xx}$ vs $V_g$ depending on the $V_g$ sweeping history and direction is observed. This hysteresis is common for STO due to its nonlinear dielectric response close to ferroelectricity[42] and may also relate to the interface charge traps (defects) between STO and TI film. Here, curve "1" (where $V_{CNP} \sim 12$ V) represents the first $V_g$ sweep from $-60$ V to 60 V after initial cooling down to 1.4 K. The corresponding $R_{xx}$ in curve "1" is consistent with the $R_{xx}$ values (shown as boxes with crosses in Fig. 1d) at each $V_g$ extracted from Fig. 1c at 1.4 K. However, $V_{CNP}$ is shifted to 50 V (curve "2") and 43 V (curve "3") as $V_g$ sweeps backward (from 60 V to $-60$ V) and forward again, respectively. Repeating the $V_g$ sweeps from 60 V to $-60$ V (or $-60$ V to 60 V), the FE curve will stabilize and follow the curve "2" (or "3"), respectively. All the data presented later are taken after this stabilization and in a forward sweeping direction to minimize this hysteresis effect (also because of this hysteresis, one should not directly compare the $V_g$'s in the following data with those in Fig. 1c, instead $V_g$-$V_{CNP}$ or low-$T$ resistance values are better indicators of the sample state). The ambipolar FE in Fig. 1d suggests a sign change of dominant charge carrier from p-type to n-type as $V_g$ crosses $V_{CNP}$, confirmed by the corresponding gate-dependent Hall resistance $R_{xy}$ (exhibiting a sign change) and $R_{xx}$ measured at $B = -6$ T as shown in Fig. 1e. We note that the charge carriers are holes at $V_g = 0$ V, also consistent with the ARPES-measured $E_f$ position in as-grown films[12]. We point out that the measured $V_{CNP}$ should be understood as an *average* global CNP for the whole sample, as the local CNP (Dirac point, DP, of the surface band) position in energy may differ between the top and bottom surfaces (as exemplified in Fig. 1c inset) and also further have spatial fluctuations (leading to electron and hole puddles). Such charge inhomogeneity (common in TI[45] as well as in graphene[46,47]) can easily make the minimum sheet conductance (2D conductivity) observed near the global CNP (~6 $e^2/h$ combining both surfaces in our sample, Fig. 1d) notably higher than the theoretically expected minimum conductivity of Dirac fermions[45–47].

**Gate and temperature dependent magnetoresistance, Hall effect, carrier density and mobility.** Figure 2 shows the gate-dependent $\Delta R_{xx}$ and the corresponding $R_{xy}$ (plotted as functions of $B$) at various temperatures (see also Fig. S2). Here, we define $\Delta R_{xx}(B) = R_{xx}(B) - R_{xx}(B = 0\ T)$. In Fig. 2(a), all curves of $\Delta R_{xx}(B)$ obtained at different $V_g$ at $T = 1.4$ K show a gate-dependent cusp at $|B| < 1.5$ T, a clear signature of the WAL. The amplitude of the cusp can be significantly enhanced by varying $V_g$ from $-60$ V to 60 V to tune $E_f$ from BVB to TSS, and reaches a maximum at CNP. Another interesting observation is the LMR observed at higher $B$ field in $\Delta R_{xx}(B)$, which is also strongly enhanced by gating towards TSS and will be discussed in detail later. Meanwhile, the corresponding

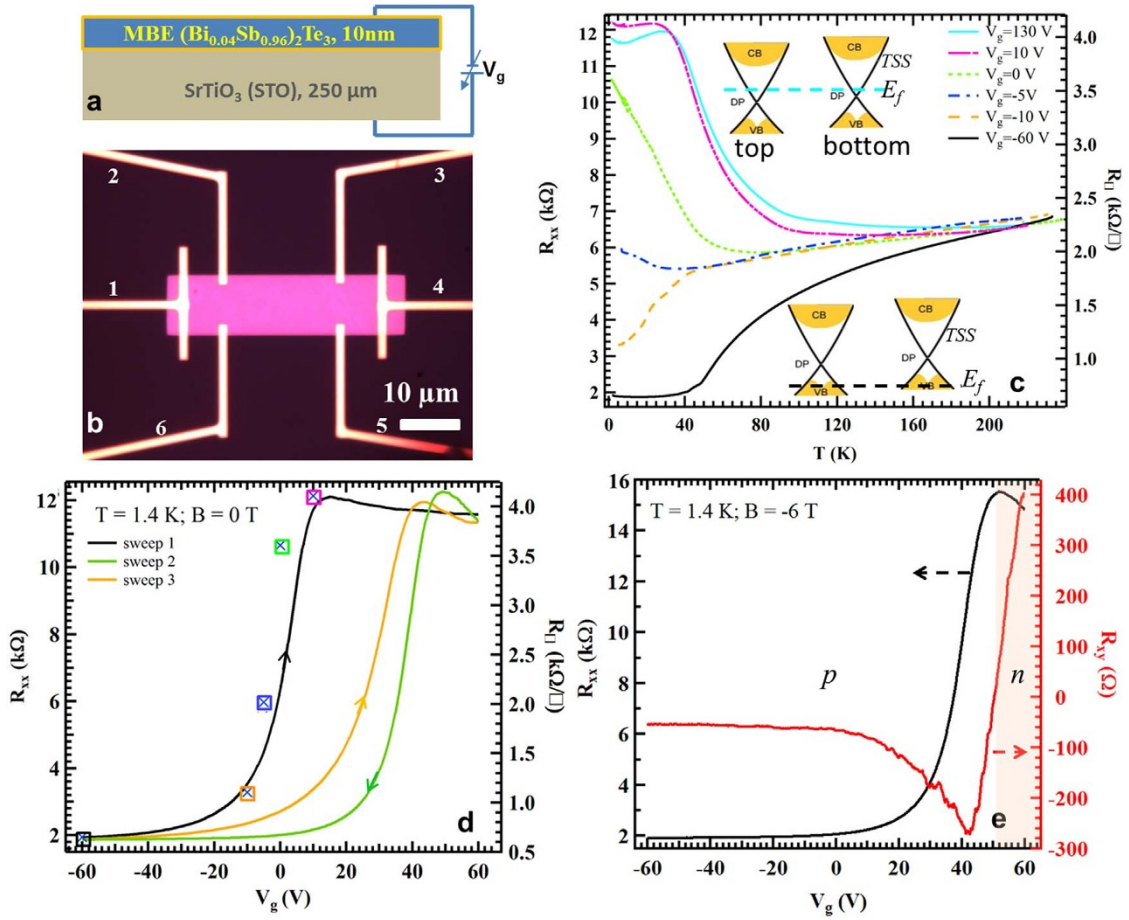


**Figure 1 | $(Bi_{0.04}Sb_{0.96})_2Te_3$ field effect device and its temperature and gate dependent transport.** (a) Schematic of MBE-grown $(Bi_{0.04}Sb_{0.96})_2Te_3$ thin films (thickness = 10 nm) on $SrTiO_3$ (STO, thickness = 250 μm, used as back gate); (b) Optical image of a fabricated Hall bar shaped device; (c) Temperature-dependent $R_{xx}$ (left axis, with corresponding $R_{xx}$ per square, $R_{\square}$, plotted on the right axis) curves at various different $V_g$. All the curves are measured at zero magnetic field ($B$) and during the cooling process. The upper and lower insets show the schematic band structure with different Fermi level ($E_f$) positions for $V_g$ = 130 V and −60 V, respectively; (d) $R_{xx}$ (left axis, with corresponding $R_{\square}$, plotted on the right axis) as a function of gate voltage ($V_g$) for different $V_g$ sweeping histories (all measured at $B$ = 0 T). The arrows label the $V_g$ sweeping directions. The symbols (boxes with crosses inside) label the resistances extracted from (c) for each $V_g$ at 1.4 K; (e) $R_{xx}$ and $R_{xy}$ as functions of $V_g$ at $B$ = −6 T and $T$ = 1.4 K. The unshaded (shaded) areas mark the $V_g$ ranges with $p$ ($n$) type dominant carriers.

$R_{xy}$ vs $B$ also shows a strong gate dependence (lower panel of Fig. 2a) with two main observations with increasing $V_g$: 1) the slope of $R_{xy}$ vs $B$ initially increases and is followed by a drop as well as a sign change while $V_g$ crosses the CNP, a direct manifestation of the sign change of charge carriers; 2) the corresponding shape of $R_{xy}$ vs $B$ changes from linear to non-linear, suggesting a change from one-band to two (or multiple) band transport (due to coexisting surface and bulk channels of opposite carriers, and/or electron and hole puddles). The $\Delta R_{xx}$ and $R_{xy}$ also show significant temperature dependences as shown in Figs. 2b–f. As $T$ increases from 1.4 K, the WAL cusp gradually weakens and finally disappears at ~25 K, where the LMR becomes prominent and starts from very low $B$ (<~0.2 T) for most of $V_g$'s (Figs. 2c and S3). Further increasing $T$ (>~40 K), $\Delta R_{xx}(B)$ becomes parabolic at low $B$ (<2 T), which becomes increasingly evident at further elevated $T$ as shown in Figs. 2d–f, with LMR still clearly observable at higher $B$ (>2 T). The ambipolar (sign change of slope) and nonlinearity (near CNP) behaviors observed in $R_{xy}$ also become increasingly evident with increasing $T$ up to ~25 K (Figs. 2a–c). However, for $T$ > 40 K, the $R_{xy}$ vs $B$ is always linear and has no sign change (Figs. 2d–f), indicating one-band behavior with p-type carriers. We note that the gate becomes less effective as $\varepsilon_r$ of STO becomes significantly reduced[42,48] at elevated $T$ (see also Fig. S4), rendering the ambipolar FE no longer achievable. Our results map out a systematic evolution of both $R_{xx}(B, V_g, T)$ and $R_{xy}(B, V_g, T)$, demonstrating the transport properties in such system are highly dependent on $E_f$ (modulated by gating) and the temperature.

Further studies of the field and Hall effects as well as $n$ and mobility are presented in Fig. 3. Figs. 3a,b show the temperature dependences of $R_{xx}$ vs $V_g$ (at $B$ = 0 T) and $R_{xy}$ vs $V_g$ (at $B$ = −6 T), respectively. Consistent with Fig. 2, for $T$ up to ~25 K, we see again the ambipolar FE (Fig. 3a) while $V_{CNP}$ increases from 45 V (at 1.4 K) to 80 V (at 25 K), related to the decreased $\varepsilon_r$ of STO substrate mentioned above[42]. The corresponding $R_{xy}$ (Fig. 3b) also demonstrates the ambipolar behavior up to ~25 K, where $R_{xy}$ (initially negative) decreases with increasing $V_g$, followed by an upturn and sign change as $V_g$ crosses CNP. For $T$ > 40 K, both $R_{xx}$ and $|R_{xy}|$ monotonously and weakly increase as $V_g$ increases with no indication of ambipolar behavior. We extract $n$ and Hall mobility ($\mu$) from $R_{xy}$ and $R_{xx}$ (in Fig. 2) using the one-band model at different $V_g$ and $T$ in the regime of p-type carriers (mostly from BVB, see below) where a linear $R_{xy}$ vs $B$ is observed, and plot the results in Figs. 3c,d. The carrier (holes) density ($n_p$) is ~$1.8 \times 10^{14}$ cm$^{-2}$ at $V_g$ = −60 V & $T$ = 1.4 K. As $V_g$ increases and approaches CNP, $n_p$ decreases approximately linearly. The similar trend is also observed at higher $T$'s up to 25 K, while the slope of $n_p$ vs $V_g$ decreases significantly with $T$ > 25 K. An effective capacitance ($C$) per unit area of STO can be calculated from the slope and $C$ decreases from ~290 nF/cm$^2$ ($\varepsilon_r$ ~ 82000) at 1.4 K down to ~5.3 nF/cm$^2$ ($\varepsilon_r$ ~ 1500) at 200 K (see Fig. S4), consistent with

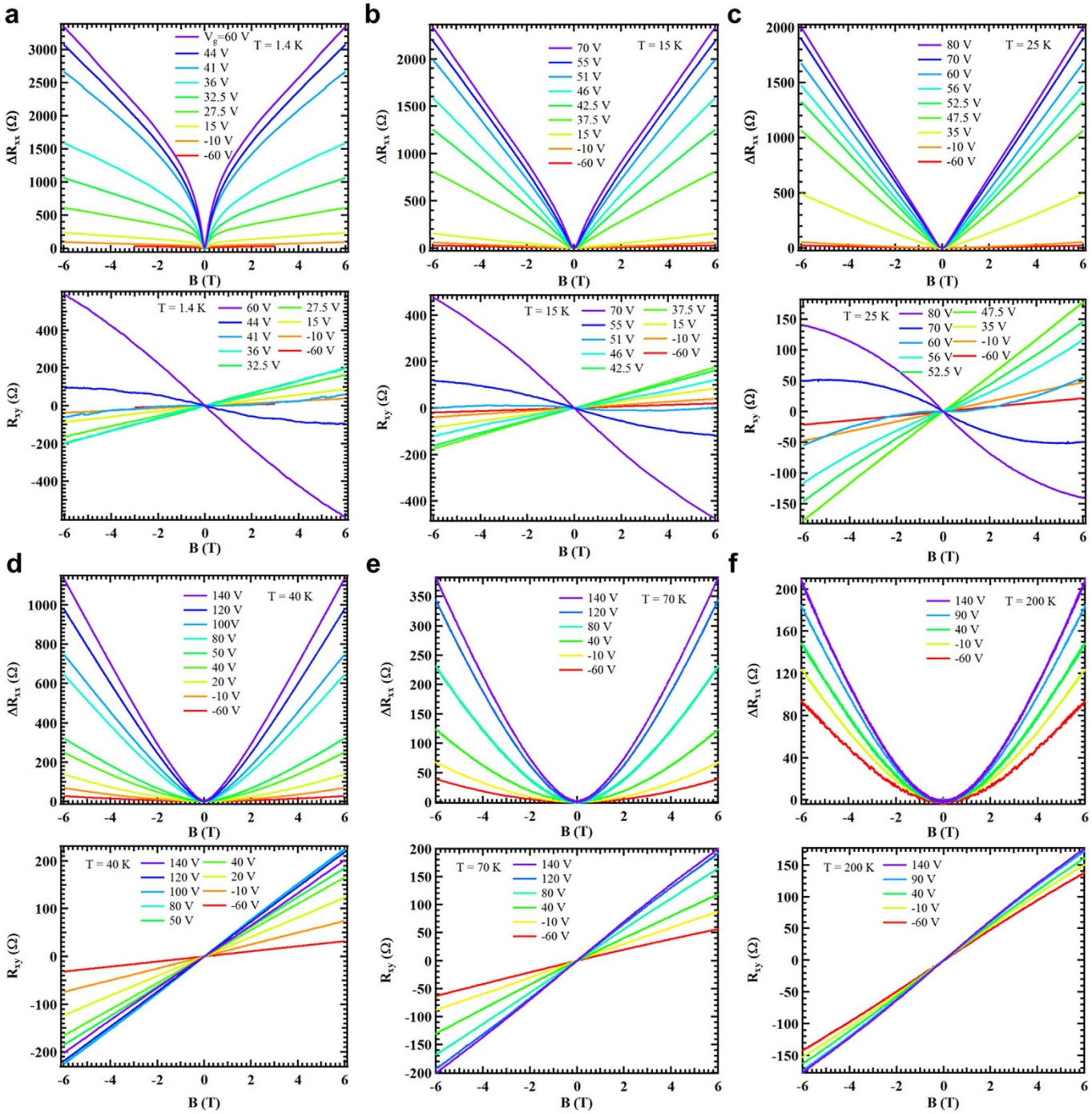


**Figure 2 | Magnetoresistance ($\Delta R_{xx} = R_{xx}(B)-R_{xx}(B = 0T)$) and Hall resistance $R_{xy}$ vs $B$ for different $V_g$ at various temperatures.** (a) $T = 1.4$ K; (b) $T = 15$ K; (c) $T = 25$ K; (d) $T = 40$ K; (e) $T = 70$ K; (f) $T = 200$ K.

previously observed strongly $T$-dependent dielectric behavior of STO[42,48]. We also note that $n_p$ at $V_g = 0$ V (Fig. 3c) decreases with increasing $T$. This is attributed to thermal excitation of $n$-type carriers, and confirms that the increased $V_{CNP}$ at higher $T$ (in Fig. 3a) is mainly due to the decreased STO capacitance. The temperature and gate-dependent $\mu$ is shown in Fig. 3d. The mobility at 1.4 K increases with increasing $V_g$ from ~50 cm$^2$/Vs at $V_g = -60$ V to ~140 cm$^2$/Vs at $V_g = 30$ V. The similar behavior is observed up to 40 K, while for T > 70 K, $\mu$ becomes ~110 cm$^2$/Vs and largely $V_g$ independent. The inset of Fig. 3d shows a summary of $\mu$ (in log scale) vs $n_p$ for all measured $T$'s, where the data appear to collapse together and can be fitted to $\mu \sim \mu_0 e^{-n_p/n_0}$ with $n_0 = 6 \times 10^{15}$ cm$^{-2}$, $\mu_0 = 133.4$ cm$^2$/Vs, suggesting that $\mu$ is mainly controlled by $n$ but not $T$ (up to ~200 K) in our system. The measured density-dependent mobility may provide valuable input for understanding carrier transport and scattering mechanism in TIs[49–52], important for developing TI-based devices. In the case where $R_{xy}$ is nonlinear with $B$ (seen in Fig. 2) due to multiple conduction channels and coexisting holes and electrons, the one-band model will not yield accurate $n$ (in Fig. S5, $n$ calculated from such one-band fits starts to deviate from linear $V_g$-dependence close to CNP). While a multiple-band model[11,17,43,53] can in principle be applied to fit the non-linear $R_{xy}$, we found however, such an analysis does not give unique fitting results (yielding significant uncertainties) in our case. Applying one-band model fitting (Fig. S5) for our data measured at T = 1.4 K, the lowest carrier (electron) density $|n|$ achieved in our sample is ~5.5 × 10$^{12}$ cm$^{-2}$

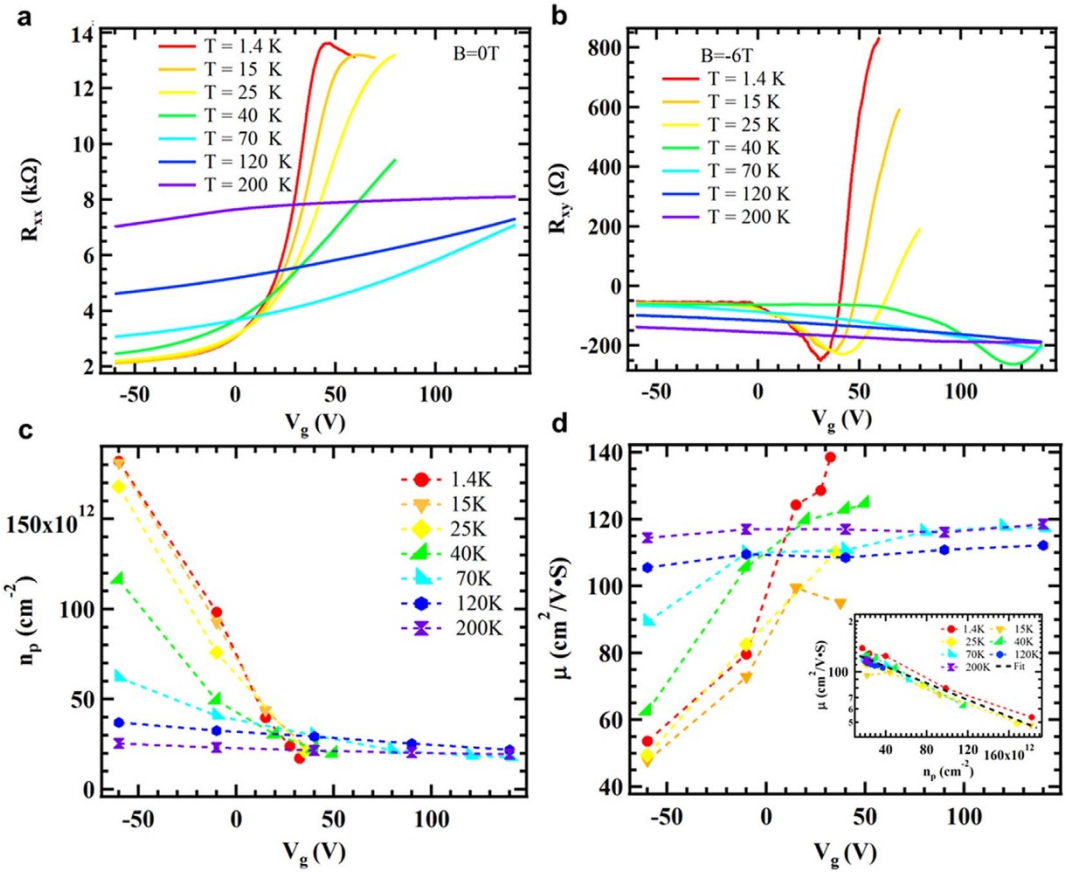


**Figure 3 | Field effect and gate-dependent carrier density ($n_p$) and mobility ($\mu$) at various temperatures.** Temperature dependences of (a) longitudinal resistance $R_{xx}$ vs $V_g$ measured at $B = 0$ T and (b) Hall resistance $R_{xy}$ vs $V_g$ measured at $B = -6$ T; (c) The carrier (hole) density $n_p$ and; (d) mobility μ extracted using a 1-band model from Fig. 2 at gate voltages where a linear Hall effect is observed. Inset is $\mu$ (in log scale) vs $n_p$ at different temperatures. Dashed line is an exponential fit ($\mu = \mu_0 e^{-n_p/n_0}$) to all data points with $n_0 = 6 \times 10^{15}$ cm$^{-2}$, $\mu_0 = 133.4$ cm$^2$/Vs.

(an *overestimate* for the actual density) at $V_g = 60$ V (where $R_{xy}$ is n-type and only slightly non-linear). This value is smaller than the estimated maximum electron density (>1.2 × 10$^{13}$ cm$^{-2}$, see Fig. S5 caption for more details) that can be accommodated in the TSS before populating BCB, demonstrating that $E_f$ is already located in the upper part (above DP) of the TSS at $V_g = 60$ V, $T = 1.4$ K. This also demonstrates that we can reach a regime where the charge carriers are mostly from the TSS and band bending near the surface is not significant to populate the bulk carriers (otherwise such a low $n$ will not be reached). The corresponding $n$ vs $V_g$ at low $T$ (Fig. S5) demonstrates that we have successfully tuned $E_f$ from the BVB, to the lower and the upper parts of TSS (through DP), as the $V_g$ is increased from −60 V to 60 V.

**Gate and temperature dependent WAL and its enhancement near CNP with two decoupled coherent surfaces.** Now we present the gate and temperature effects on the WAL, which is a manifestation of quantum coherent transport in the low-$B$ MR and observed in our sample below 15 K. Figure 4a shows the sheet conductance correction $\Delta G_{\square}(B) = G_{\square}(B) - G_{\square}(B = 0T)$ vs $B$ at various $V_g$'s measured at 1.4 K, where $G_{\square} = (L/W)/R_{xx}$ with $W$ and $L$ being the width and length of the channel (between voltage probes) respectively. While both the bulk and TSS of TI possess strong spin-orbit coupling and can give rise to WAL, we have observed that WAL is significantly enhanced as $E_f$ is tuned into the BBG to suppress the bulk conduction and decouple the top and bottom surfaces. The Hikami-Larkin-Nagaoka (HLN)[54] equation (1) has been widely applied to analyze $\Delta G_{\square}(B)$ due to WAL:

$$\Delta G_{\square}(B) \simeq \alpha \frac{e^2}{\pi h}\left[\psi\left(\frac{1}{2}+\frac{B_\phi}{B}\right) - \ln\left(\frac{B_\phi}{B}\right)\right] \quad (1)$$

where $\alpha$ is a prefactor expected to be -1/2 for a single coherent channel, $\psi$ is the digamma function, and $B_\phi = \hbar / 4eL_\phi^2$ is a characteristic field (with $L_\phi = \sqrt{D\tau_\phi}$, the phase coherence length, and $\tau_\phi$ phase-coherence time, $D$ the diffusion constant). It is found[22] that even with parallel conducting channels (such as bulk and surfaces), the total $\Delta G_{\square}$ may still be fitted using Eq. (1) in terms of an effective $\alpha$ that reflects the inter-channel coupling (with $A = 2|\alpha|$ representing the effective number of coherent channels). Our data in Fig. 4a agrees well (up to 2 T) with the HLN fittings (see Fig. S6). The extracted values of $|\alpha|$ ($\alpha < 0$) and $L_\phi$ at various $V_g$'s and temperatures are shown in Figs. 4b–c, respectively. We find that $|\alpha|$ is strongly gate-tunable and exhibits an "ambipolar" behavior (peaks ~ 1 at CNP) for all $T$'s where WAL is observed, revealing three regimes of behavior as the number of coherent channels and degree of inter-channel coupling are tuned by the gate: (I) $V_g < -10$ V, where $E_f$ is in the BVB, $|\alpha| \sim 0.5$ indicates the surface and bulk are fully coupled into one coherent conduction channel ($A \sim 1$); (II) As $V_g$ is increased ($-10$ V $< V_g < +45$ V) to lift $E_f$ toward the BBG (TSS), $|\alpha|$ (and A) increases, indicating the top and bottom surfaces start to decouple from the bulk and each other, toward forming two channels; when $V_g$ reaches ~45 V, where the $E_f$ is close to CNP, $|\alpha|$ reaches a maximum ~1 = |−(1/2 + 1/2)|) with $A \sim 2$, corresponding to two fully separated phase coherent channels (surrounding the bottom and top surfaces); (III) Further increasing $V_g > 45$ V to increase the $E_f$

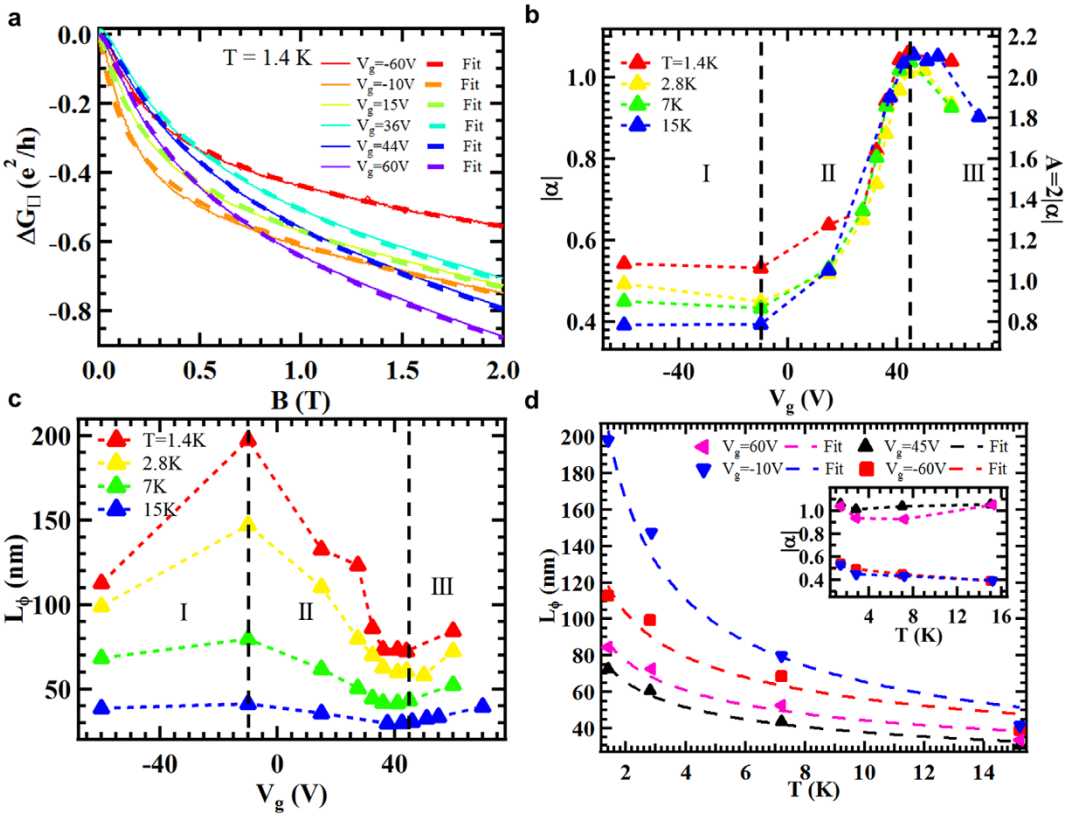


**Figure 4 | Gate and temperature dependent weak antilocalization (WAL) effect.** (a) Gate dependence of sheet conductance ($\Delta G_{\square} = G_{\square}(B)$-$G_{\square}(B = 0T)$) at 1.4 K for various $V_g$'s. The dashed curves are fits to the data using the HLN model (Eq. 1); Gate dependent (b) prefactor $|\alpha| = -\alpha$ (A = 2|α|, right axis, is the number of coherent conducting channels) and (c) phase coherence length $L_\varphi$ extracted from Eq. (1) at various temperatures; (d) Temperature dependence of $L_\varphi$ and (inset) |α| measured at four representative $V_g$ = 60 V, 45 V, −10 V and −60 V. Dashed lines in the main panel (for $L_\varphi$) are power law fittings (see text).

above the CNP in TSS and towards BCB, |α| starts to decrease from 1, indicating the top and bottom surfaces start to be coupled again. Our analysis also suggests that care must be taken when attributing WAL to TSS (especially for $\alpha \sim -0.5$)[19,24–27] in a TI material with both bulk and surface conduction. In addition, we find that the phase coherent length $L_\phi$ also shows interesting gate dependence (Fig. 4c). In regime I, in contrast to the weak gate dependence of |α|, $L_\phi$ at low $T$ (1.4 and 2.8 K) notably increases with increasing $V_g$ and peaks at $V_g$ = −10 V. Between regimes II and III, $L_\phi$ reaches a local minimum when $V_g$ is near CNP, where |α| reaches a peak.

Figs. 4b–c also demonstrate the temperature dependence of |α| and $L_\phi$ in different regimes of $V_g$. We see that in regimes II and III, |α| is relatively insensitive to $T$. In regime I, |α| moderately decreases below 0.5 with increasing $T$ when the TSS is coupled to the bulk at $V_g$ = −60 V and −10 V, similar to the behavior previously found in samples with bulk-dominated conduction and explained as the suppression of WAL at high $T$[22]. Fig. 4d shows the temperature dependences of $L_\phi$ at 4 representative $V_g$'s. Previous studies have commonly fitted $L_\phi(T)$ to a power-law, with the expectation that electron-electron scattering would give $L_\phi$ proportional to $T^{-0.5}$ (or $T^{-0.75}$) in a 2D (or 3D) system[44,55,56]. In Fig. 4d, such power-law fittings give $L_\phi$ proportional to $T^{-0.38}$, $T^{-0.57}$, $T^{-0.34}$, and $T^{-0.34}$ for $V_g$ = −60 V, −10 V, +45 V and +60 V. We note that the fitted power-law $T$-dependences of $L_\phi$ in previous experiments range from $T^{-0.24}$ (Ref. 57 ), $T^{-0.5}$ (Refs. 44, 58 ) to $T^{-0.75}$ (Ref. 22) for different TI thin films, and $\sim T^{-0.37}$ (Refs. 59, 60 ) or $T^{-0.5}$ (Refs. 61, 62 ) for TI nanowires, suggesting that the observed power-law can depend on detailed material or electronic properties, possibly related to other dephasing processes (not just electron-electron scattering), therefore a gate-dependence as we see may not be unexpected. In our case, only at $V_g$ = −10 V (where $L_\phi$ is also the largest, Fig. 4c) we observe $L_\phi \sim T^{-0.5}$, close to the predicted behavior of electron dephasing due to electron-electron scattering in 2D. However, strong deviation from this behavior is observed for other $V_g$'s, where $L_\phi$ is also shorter (for $V_g$ = −60 V, $L_\phi \sim T^{-0.38}$, where only one coupled 2D conduction channel exists; for $V_g$ = 45 V, where there are 2 decoupled conduction channels, and 60 V, both giving $L_\phi \sim T^{-0.34}$), suggesting existence of additional dephasing processes at these $V_g$'s (such processes may be related to other carrier pockets in the valence band for $V_g$ = −60 V; and electron-hole puddles near CNP for $V_g$ = 45 and 60 V).

**Gate and temperature tunable LMR and its enhancement near CNP.** We now discuss the pronounced LMR observed. In contrast to the standard quadratic MR[41], the observed LMR does not seem to saturate in high fields. Figs. 5a–d show the temperature-dependent LMR and corresponding $R_{xy}$ at two representative $V_g$'s. The LMR (at 6 T) in terms of relative MR ($\Delta R_{xx}(B)/R_{xx}(B = 0T)$) varies from a few percent to ~30% depending on $V_g$ and $T$. We note the high-$B$ (>2T) MR to be slightly sub-linear (super-linear) for $T < 25$ K ($T > 25$ K) with the 25 K MR being closest to strictly linear (Figs. 5a,c and Fig. 2). Figure 5e shows the slope ($k$) of LMR (extracted between 3 T and 6 T) vs $V_g$ at different temperatures. When $E_f$ is in BVB ($V_g < 0$ V), $k$ has very little $T$-dependence and weakly increases with increasing $V_g$, whereas $k$ is dramatically enhanced (by as much as 10 times, and becomes much more $T$-dependent) and approaches a maximum near CNP as $E_f$ is tuned into BBG (TSS) at low $T$. Such an observation is confirmed by the temperature dependence of $k$ at five $V_g$'s plotted in Fig. 5f. For $V_g$ = −60 V and −10 V, where $E_f$'s are located in the BVB, $k$ has little temperature dependence in the measured $T$ range. As $E_f$ is tuned into the BBG (TSS), $k$ dramatically

increases with the decreasing $T$ and reaches the highest value near CNP at $T = 1.4$ K. Interestingly, as plotted in the inset of Fig. 5f, we find that $k$ vs $n_p$ (in log-log scale, only including data points with one-band $n_p$ for holes as those included in Fig. 3c) at different temperatures follow a similar trend with $k$ approximately proportional to $n_p^{-1}$ (except for the data at 200 K), suggesting that the carrier density is important to control $k$, which is significantly enhanced as $E_f$ approaches TSS (see Fig. S8). We note that, at a fixed $n_p$, $k$ shows little $T$ dependence up to 25 K, while $k$ notably decreases with increasing $T$ for $T > 25$ K (Fig. S8). In the n-type regime (close to CNP), the large LMR is accompanied by prominent nonlinearity in $R_{xy}$ (Fig. 5d and Fig. 2c). This observation suggests that charge inhomogeneity may play an important role in the enhanced LMR, as discussed further below.

## Discussion

**Further understanding of gate-tuned WAL.** Our gate tunable WAL can also be understood[22] in terms of a competition between the phase coherence time ($\tau_\varphi$, which does not vary strongly with the $V_g$, Fig. S7) and the surface-to-bulk scattering time[22] ($\tau_{SB}$, which decreases with increasing $n$[63]), where the effective $|\alpha|$ generally increases with increasing $\tau_{SB}/\tau_\varphi$[22] as $V_g$ is tuned towards CNP. When the $E_f$ is in the BVB, $\tau_\varphi$ (~hundreds of ps, Fig. S7) is much larger than $\tau_{SB}$ ($\ll$1ps[63]), resulting in a single phase coherent channel. As $E_f$ is tuned into the TSS, $\tau_{SB}$ significantly increases due to the reduced $n$ and bulk conduction, and ultimately can become larger than $\tau_\varphi$, realizing two-decoupled channels. The weak increase of $|\alpha|$ at higher $T$ in regimes II and III seen in the inset of Fig. 4d may be attributed to a decrease in $\tau_\varphi/\tau_{SB}$, which increases the inter-channel decoupling, given that both $L_\phi$ and $\tau_\varphi \sim L_\phi^2$ decreases as $T$ increases (Fig. S7) while the $\tau_{SB}$ should be relatively constant as both $R$ and $n$ (Figs. 1c & 3c) change little up to ~15 K. However, in regime I, $|\alpha|$ moderately decreases below 0.5 at higher $T$, where $\tau_{SB}$ is expected to be much shorter than $\tau_\varphi$ in the measured temperature range[22]. Such a decrease of $|\alpha|$ below 0.5 in presence of strong bulk conduction has been attributed to WAL getting suppressed when $\tau_\varphi$ decreases and becomes comparable to the spin-orbit scattering time $\tau_{SO}$ at higher $T$[22].

**Understanding LMR.** There have been two common models proposed for the LMR, the classical model by Parish-Littlewood (PL)[38,39] and the quantum model by Abrikosov[40,41]. According to the quantum model[40,41], a LMR would occur at the quantum limit where the applied magnetic field is so large that only one[40,41] or few[36] Landau levels (LLs) are populated. This condition is more easily satisfied in a gapless semiconductor with linear energy-momentum dispersion[40,41]. The theory also predicts that $\Delta R_{xx}$ (magnitude of LMR) is proportional to $1/n^2$ and has no direct dependence on $T$ (as long as $T$ remains lower than the energy gap between LLs and the $E_f$). More recently, another model by Wang & Lei, based on the TSS and assuming uniform $n$, relaxes the requirement of extreme quantum limit (instead assuming many LLs are filled and smeared by disorder) and predicts a LMR with $\Delta R_{xx} \propto 1/n$[64]. On the other hand, Parish and Littlewood proposed a classical mechanism for the LMR, as a consequence of potential and mobility fluctuations in an inhomogeneous electronic system, resulting in admixture of Hall resistance into $R_{xx}$ on a microscopic level and a LMR[38,39]. The classical model predicts that the relative MR $= \Delta R_{xx}/R_{xx}(B = 0T)$ (thus slope $k$) should be proportional to a mobility scale $\mu_S = \max(|\mu|,|\Delta\mu|)$, where $\mu$ is mobility and $\Delta\mu$ is the mobility fluctuation, and the cross over field $B_C$ (the magnetic field at which the MR curve changes from parabolic to linear) is proportional to $1/\mu_S$. The previously reported LMR in TIs have been often interpreted in terms of the quantum model[40,41] based on the linear dispersion of the TSS[30,32]. However, the studies reported so far have not systematically measured the dependence of LMR on $n$, $\mu$ and $T$, while such information is important to unambiguously identify and distinguish different mechanisms for LMR as discussed above. It also remains unclear whether bulk and surface carriers may contribute differently to LMR. We find that none of the existing models can fully explain our observed LMR. For example, in the p-type one-band carrier regime (inset of Fig. 5f), where $E_f$ is in the BVB (because the lowest $n_p$ ($1.7 \times 10^{13}$ cm$^{-2}$) extracted here is higher than the estimated maximum hole density ($1.2 \times 10^{13}$ cm$^{-2}$) that can be accommodated in the TSS before populating BVB), we are far from the extreme quantum limit (with LMR observable at very high LL filling factor, eg. >8,000) assumed in Abrikosov's quantum model, and the assumptions of linear band dispersion or TSS as invoked by Abrikosov[41] or used in Wang-Lei model also do not apply. We have plotted the LMR amplitude (by $\delta R_{xx} = R_{xx}(6T)$-$R_{xx}(3T)$, focusing on the $B > 3$T regime where LMR is fully developed) vs $n_p$ (Fig. S9) and found it cannot be fitted to a single power-law (either $1/n_p^2$ (Abrikosov) or $1/n_p$ (Wang-Lei)) over this density range, but rather appears to cross over from a $\sim 1/n_p$ behavior for $n_p > 4 \times 10^{13}$ cm$^{-2}$ to $\sim 1/n_p^2$ behavior for $n_p < 4 \times 10^{13}$ cm$^{-2}$ (except for the data at 200K). As $E_f$ is tuned into the TSS or CNP, the LMR is enhanced and shows strong $T$-dependence (see Figs. 5e,f and S9a,b), while concurrently $R_{xy}(B)$ becomes strongly non-linear (Fig. 5d, also Fig. 2c) and exhibits a sign-change (carrier type inversion), indicating charge inhomogeneity (such as coexisting electron and hole puddles) is significant in this ambipolar regime. This is at odds with the $T$-independent LMR predicted in both Abrikosov's quantum model and the Wang-Lei model (which also assumes uniformly distributed charge carriers), but instead suggests that charge inhomegeity (as highlighted in the classical mechanism) may play important roles in the LMR. To address the question whether the classical model can describe our observed LMR (in both BVB and TSS regimes), it is important to examine the correlation between $k$, $B_C$, and $\mu$ (Figs. S10–S12). In the BVB regime (where p-type carrier $\mu$ can be extracted from one-band model), we find that $k$ appears to be approximately proportional to $\mu$ (consistent with PL model prediction if $\mu_s \sim \mu$) up to $\mu \sim 100$ cm$^2$/Vs, but becomes poorly correlated with $\mu$ for higher $\mu$ (Fig. S10). Fig. S11 shows $B_C$ as a function of $\mu$, which is *qualitatively* ($B_C$ generally lower for larger $\mu$) but not quantitatively consistent with the PL model (predicting $1/B_C$ to be proportional to $\mu$, if $\mu_s \sim \mu$). Furthermore, we note that PL model should predict $1/B_C$ to be proportional to $k$ (even without direct knowledge of $\mu_s$, which could depend on $\Delta\mu$). We have examined the correlation between $1/B_C$ and $k$ (Fig. S12) and find that while such a proportionality may hold approximately at relatively high $T$ (>40K), it does not hold for the full data set (including the 25K data, where LMR is particularly pronounced). In any case, our systematic data have revealed the following important points: 1) TSS can strongly enhance the LMR; 2) the charge inhomogeneity also plays important roles in the observed LMR, whose behaviors appear to be *qualitatively* captured by the classical model but several aspects are still *not quantitatively* accounted for. A more complete model likely needs to take into account both the full band structure (bulk and TSS) and inhomogeneity in order to fully explain the observed LMR. Our systematic results on the density, mobility, and temperature dependences of LMR (Figs. 5 and S8–12) can provide important insights for understanding the mechanisms of LMR and key inputs to develop a more complete model.

## Methods

**Material synthesis.** The high quality $(Bi_{0.04}Sb_{0.96})_2Te_3$ (10 nm-thick) thin films studied here are grown by MBE on heat-treated 250μm-thick insulating STO (111) substrates[12]. The schematic of the sample is shown in Fig. 1a. Previous ARPES measurements have demonstrated that the TSS exists in the BBG and the $E_f$ is located below the Dirac point, indicating a p-type doping in the as-grown films[12].

**Device fabrication and transport measurements.** The representative device structures are defined by standard e-beam lithography (EBL), followed by dry etching

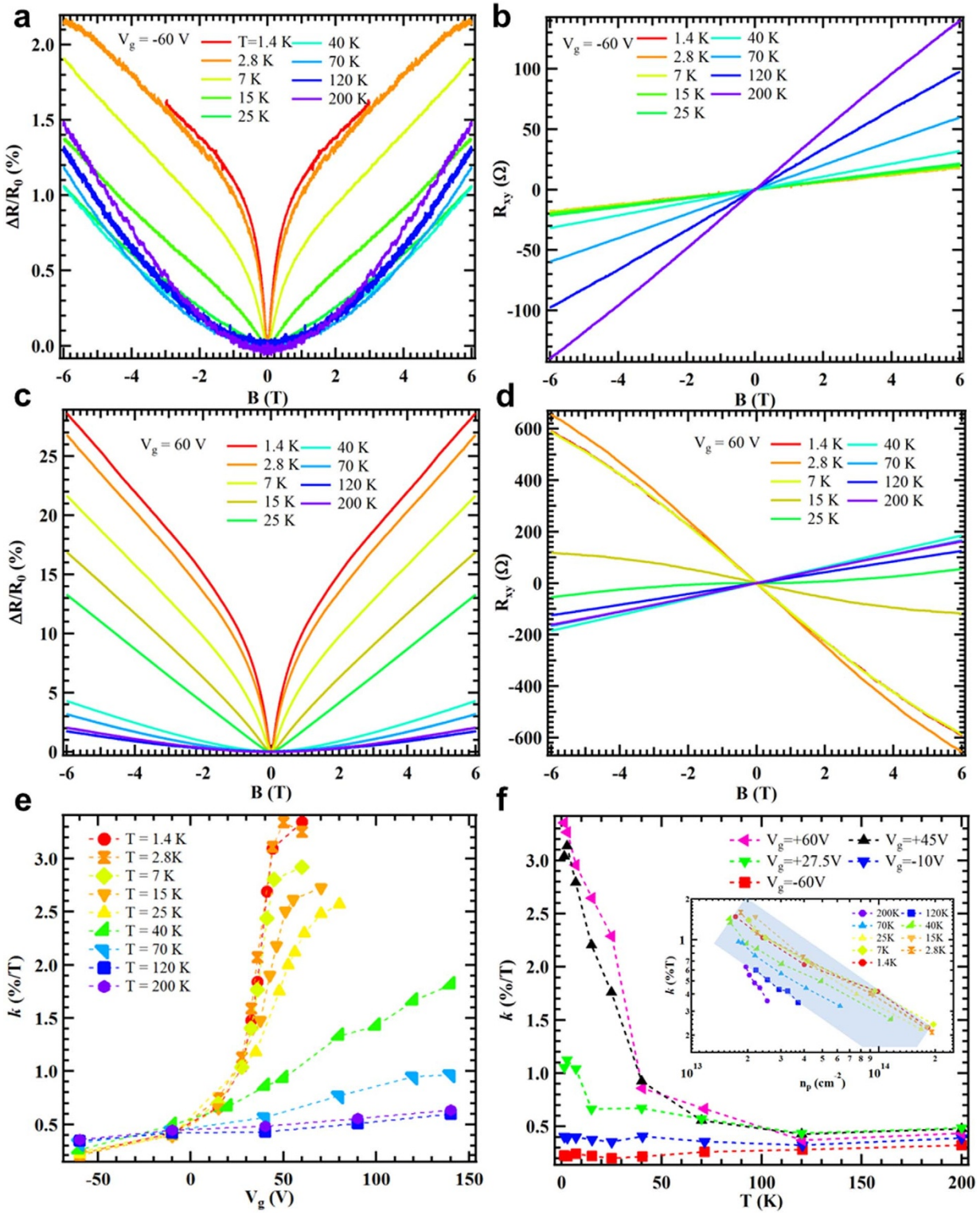


**Figure 5 | Gate and temperature tunable linear magnetoresistance (LMR).** The LMR, $\Delta R_{xx}/R_{xx}(B = 0T)$, and the corresponding $R_{xy}$ as functions of magnetic field $B$ at (a,b) $V_g = -60$ V and (c,d) $V_g = 60$ V measured at various temperatures (ranging from 1.4 K to 200 K), respectively; (e) The gate voltage dependence of the extracted LMR slope ($k$, extracted between 3 T and 6 T) at different temperatures; (f) The LMR slope ($k$) vs $T$ for different gate voltages. Inset shows $k$ vs $n_p$ (in log-log scale) at different temperatures for $n_p$ values shown in Fig. 3c (one band p-type carriers). Gray band indicates a power law with exponent $-1$ ($k \sim n_p^{-1}$). The data for $T = 200$ K can be fitted by $\sim n_p^{-2}$.

using Ar plasma. The Hall bar electrodes of the devices are fabricated by another EBL process followed by e-beam deposition of Cr/Au (5/80 nm). A Cr/Au (5/100 nm) film is e-beam deposited on the back of the STO substrate working as a back gate. Transport properties are measured by the conventional four-probe lock-in technique with an AC driving current of 100 nA at 17.77 Hz. In a typical device (shown in Fig 1b), the driving current is applied between electrodes "1,4" and the longitudinal resistance $R_{xx}$ and Hall resistance $R_{xy}$ are measured between electrodes "5,6" and "3,5", respectively. All the measurements are carried out in a variable temperature ($T$, from 1.4 K to 230 K) cryostat with a magnetic field $B$ (perpendicular to the film) up to $\pm 6$ T.

1. Hasan, M. Z. & Kane, C. L. Colloquium: topological insulators. *Rev. Mod. Phys.* **82**, 3045–3067 (2010).
2. Qi, X.-L. & Zhang, S.-C. Topological insulators and superconductors. *Rev. Mod. Phys.* **83**, 1057–1110 (2011).
3. Yazyev, O. V., Moore, J. E. & Louie, S. G. Spin polarization and transport of surface states in the topological insulators $Bi_2Se_3$ and $Bi_2Te_3$ from first principles. *Phys. Rev. Lett.* **105**, 266806 (2010).
4. Fu, L. & Kane, C. L. Superconducting proximity effect and Majorana fermions at the surface of a topological insulator. *Phys. Rev. Lett.* **100**, 096407 (2008).
5. Linder, J., Tanaka, Y., Yokoyama, T., Sudbø, A. & Nagaosa, N. Unconventional superconductivity on a topological insulator. *Phys. Rev. Lett.*, **104**, 067001 (2010).
6. Seradjeh, B., Moore, J. E. & Franz, M. Exciton condensation and charge fractionalization in a topological insulator film. *Phys. Rev. Lett.* **103**, 066402 (2009).
7. Qi, X.-L., Hughes, T. L. & Zhang, S.-C. Topological field theory of time-reversal invariant insulators. *Phys. Rev. B.* **78**, 195424 (2008).
8. Zhang, H. *et al.* Topological insulators in $Bi_2Se_3$, $Bi_2Te_3$ and $Sb_2Te_3$ with a single Dirac cone on the surface. *Nat. Phys.* **5**, 438–442 (2009).
9. Xia, Y. *et al.* Observation of a large-gap topological-insulator class with a single Dirac cone on the surface. *Nat. Phys.* **5**, 398–402 (2009).
10. Chechelsky, J. G. *et al.* Quantum interference in macroscopic crystals of nonmetallic $Bi_2Se_3$. *Phys. Rev. Lett.* **103**, 246601 (2009).
11. Qu, D.-X., Hor, Y. S., Xiong, J., Cava, R. J. & Ong, N. P. Quantum oscillations and Hall anomaly of surface states in the topological insulator $Bi_2Te_3$. *Science* 329, 821–824 (2010).
12. Zhang, J. *et al.* Band structure engineering in $(Bi_{1-x}Sb_x)_2Te_3$ ternary topological insulators. *Nat. Commun.* **2**, 574 (2011).
13. He, X. *et al.* Highly tunable electron transport in epitaxial topological insulator $(Bi_{1-x}Sb_x)_2Te_3$ thin films. *Appl. Phys. Lett.* **101**, 123111 (2012).
14. Chang, C.-Z. *et al.* Experimental observation of the quantum anomalous Hall effect in a magnetic topological insulator. *Science* **340**, 167–170 (2013).
15. Veldhorst, M. *et al.* Magnetotransport and induced superconductivity in Bi based three-dimensional topological insulators. *Phys. Status Solidi RRL* **7**, 26–38 (2013).
16. Taskin, A. A. *et al.* Observation of Dirac holes and electrons in a topological insulators. *Phys. Rev. Lett.* **107**, 016801 (2011).
17. Ren, Z., Tashin, A. A., Sasaki, S., Segawa, K. & Ando, Y. Large bulk resistivity and surface quantum oscillations in the topological insulator $Bi_2Te_2Se$. *Phys. Rev. B* **82**, 241306 (2010).
18. Xiong, J. *et al.* Quantum oscillations in a topological insulator $Bi_2Te_2Se$ with large bulk resistivity (6 Ωcm). *Physica E* **44**, 917–920 (2012).
19. Chen, J. *et al.* Gate-voltage control of chemical potential and weak antilocalization in $Bi_2Se_3$. *Phys. Rev. Lett.* **105**, 176602 (2010).
20. Zhang, G. *et al.* Growth of topological insulator $Bi_2Se_3$ thin films on SrTiO3 with large tunability in chemical potential. *Adv. Funct. Mater.* **21**, 2351–2355 (2011).
21. Chen, J. *et al.* Tunable surface conductivity in $Bi_2Se_3$ revealed in diffusive electron transport. *Phys. Rev. B* **83**, 241304 (2011).
22. Steinberg, H., Laloe, J. B., Fatemi, V., Moodera, J. S. & Jarillo-Herrero, P. Electrically tunable surface-to-bulk coherent coupling in topological insulator thin films. *Phys. Rev. B* **84**, 233101 (2011).
23. Checkelsky, J. G., Hor, Y. S., Cava, R. J. & Ong, N. P. Bulk band gap and surface state conduction observed in voltage-tuned crystals of the topological insulator $Bi_2Se_3$. *Phys. Rev. Lett.* **106**, 196801 (2011).
24. Kim, Y. S. *et al.* Thickness-dependent bulk properties and weak antilocalization effect in topological insulator $Bi_2Se_3$. *Phys. Rev. B* **84**, 073109 (2011).
25. Liu, M. *et al.* Electron interaction-driven insulating ground state in $Bi_2Se_3$ topological insulators in the two-dimensional limit. *Phys. Rev. B* **83**, 165440 (2011).
26. He, H.-T. *et al.* Impurity effect on weak antilocalization in the topological insulator $Bi_2Te_3$. *Phys. Rev. Lett.* **106**, 166805 (2011).
27. Wang, J. *et al.* Evidence for electron-electron interaction in topological insulator thin films. *Phys. Rev. B* **83**, 245438 (2011).
28. Taskin, A. A., Sasaki, S., Segawa, K. & Ando, Y. Manifestation of topological protection in transport properties of epitaxial $Bi_2Se_3$ thin films. *Phys. Rev. Lett.* **109**, 066803 (2012).
29. Kim, D., Syers, P., Butch, N. P., Paglione, J. & Fuhrer, M. S. Coherent topological transport on the surface of $Bi_2Se_3$. *Nat. Commun.* **4**, 2040 (2013).
30. Tang, H., Liang, D., Qiu, R. L. J. & Gao, X. P. A. Two-dimensional transport-induced linear magneto-resistance in topological insulator $Bi_2Se_3$ nanoribbons. *ACS Nano* **5**, 7510–7516 (2011).
31. Gao, B. F., Gehring, P., Burghard, M. & Kern, K. Gate-controlled linear magnetoresistance in thin $Bi_2Se_3$ sheets. *Appl. Phys. Lett.* **100**, 212402 (2012).
32. Wang, X., Du, Y., Dou, S. & Zhang, C. Room temperature giant and linear magnetoresistance in topological insulator $Bi_2Te_3$ nanosheets. *Phys. Rev. Lett.* **108**, 266806 (2012).
33. He, H. *et al.* High-field linear magneto-resistance in topological insulator $Bi_2Se_3$ thin films. *Appl. Phys. Lett.* **100**, 032105 (2012).
34. Zhang, S. X. *et al.* Magneto-resistance up to 60 tesla in topological insulator $Bi_2Te_3$ thin films. *Appl. Phys. Lett.* **101**, 202403 (2012).
35. Dresselhaus, P. D., Papavassiliou, C. M. A. & Wheeler, R. G. Observation of spin precession in GaAs inversion layers using antilocalization. *Phys. Rev. Lett.* **68**, 106–109 (1992).
36. Hu, J. S. & Rosenbaum, T. F. Classical and quantum routes to linear magnetoresistance. *Nat. Mater.* **7**, 697–700 (2008).
37. Xu, R. *et al.* Large magnetoresistance in non-magnetic silver chalcogenides. *Nature* **390**, 57–60 (1997).
38. Parish, M. M. & Littlewood, P. B. Non-saturating magnetoresistance in heavily disordered semiconductors. *Nature*, **426**, 162–165 (2003).
39. Hu, J., Parish, M. M. & Rosebaum, T. F. Nonsaturating magnetoresistance of inhomogeneous conductors: comparison of experiment and simulation. *Phys. Rev. B* **75**, 214203 (2007).
40. Abrikosov, A. A. Quantum magnetoresistance. *Phys. Rev. B* **58**, 2788–2794 (1998).
41. Abrikosov, A. A. Quantum linear magnetoresistance. *Europhys. Lett.* **49**, 789–793 (2000).
42. Gouto, N. J. G., Sacépé, B. & Morpurgo, A. F. Transport through Graphene on $SrTiO_3$. *Phys. Rev. Lett.* **107**, 225501 (2011).
43. Yu, X. *et al.* Separation of top and bottom surface conduction in $Bi_2Te_3$ thin films. *Nanotech.* **24**, 015705 (2013).
44. Cha, J. J. *et al.* Weak antilocalization in $Bi_2(Se_xTe_{1-x})_3$ nanoribbons and nanoplates. *Nano Lett.* **12**, 1107–1111 (2012).
45. Kim, D. *et al.* Surface conduction of topological Dirac electrons in bulk insulating $Bi_2Se_3$. *Nat. Phys.* **8**, 459–463 (2012).
46. Martin, J. *et al.* Observation of electron–hole puddles in graphene using a scanning single-electron transistor. *Nat. Phys.* **4**, 144–148 (2008).
47. Blake, P. *et al.* Influence of metal contacts and charge inhomogeneity on transport properties of graphene near the neutrality point. *Solid State Commun.* **149**, 1068–1071 (2009).
48. Muller, K. A. & Burkard, H. $SrTiO_3$: An intrinsic quantum paraelectric below 4 K. *Phys. Rev. B* **19**, 3593–3602 (1979).
49. Culcer, D., Hwang, E. H., Stanescu, T. D. & Das Sarma, S. Two-dimensional surface charge transport in topological insulators. *Phys. Rev. B* **82**, 155457 (2010).
50. Li, Q., Rossi, E. & Das Sarma, S. Two-dimensional electronic transport on the surface of three-dimensional topological insulators. *Phys. Rev. B* **86**, 235443 (2012).
51. Adam, S., Hwang, E. H. & Das Sarma, S. Two-dimensional transport and screening in topological insulator surface states. *Phys. Rev. B* **85**, 235413 (2012).
52. Giraud, S., Kundu, A. & Egger, R. Electron-phonon scattering in topological insulator thin films. *Phys. Rev. B* **85**, 035441 (2012).
53. He, L. *et al.* Surface-dominated conduction in a 6 nm thick $Bi_2Se_3$ Thin Film. *Nano. Lett.* **12**, 1486–1490 (2012).
54. Hikami, S., Larkin, A. I. & Nagaoka, Y. Spin-Orbit interaction and magnetoresistance in the two dimensional random system. *Prog. Theor. Phys.* **63**, 707–710 (1980).
55. Assaf, B. A. *et al.* Linear magnetoresistance in topological insulator thin films: quantum phase coherence effects at high temperatures. *Appl. Phys. Lett.* **102**, 012102 (2013).
56. Altshuler, B. L. & Aronov, A. G. *Electron-electron interaction in disordered systems. Vol. 10*, (Elsevier, New York, 1985).
57. Chiu, S.-P. & Lin, J.-J. Weak antilocalization in topological insulator $Bi_2Te_3$ microflakes. *Phys. Rev. B* **87**, 035122 (2013).
58. Takagaki, Y., Giussani, A., Perumal, K., Calarco, R. & Friedland, K.-J. Robust topological surface states in $Sb_2Te_3$ layers as seen from the weak antilocalization effect. *Phys. Rev. B* **86**, 125137 (2012).
59. Matsuo, S. *et al.* Weak antilocalization and conductance fluctuation in a submicrometer-sized wire of epitaxial $Bi_2Se_3$. *Phys. Rev. B* **85**, 075440 (2012).
60. Ning, W. *et al.* One-dimensional weak antilocalization in single-crystal $Bi_2Te_3$ nanowires. *Sci. Rep.* **3**, 1564 (2013).
61. Hamdou, B., Gooth, J., Dorn, A., Pippe, E. & Nielsch, K. Aharonov-Bohm oscillations and weak antilocalization in topological insulator $Sb_2Te_3$ nanowires. *Appl. Phys. Lett.* **102**, 223110 (2013).
62. Peng, H. *et al.* Aharonov–Bohm interference in topological insulator nanoribbons. *Nat. Mater.* **9**, 225–229 (2010).
63. Park, S. R. *et al.* Quasiparticle scattering and the protected nature of the topological states in a parent topological insulator $Bi_2Se_3$. *Phys. Rev. B* **81**, 041405 (2010).
64. Wang, C. M. & Lei, X. L. Linear magnetoresistance on the topological surface. *Phys. Rev. B* **86**, 035442 (2012).


## Acknowledgments

The work at Purdue is supported by DARPA MESO program (Grant N66001-11-1-4107). The MBE synthesis of TI thin films is supported by NSF of China (Grants 11134008 and 11174343).

## Author contributions

C.Z.C. synthesized the TI films, with advice from K.H., X.C.M. and Q.K.X. J.T. fabricated the devices, performed transport measurements and analyzed the data with assistance from H.C. and advice from Y.P.C. J.T. and Y.P.C. wrote the paper, with discussions and comments from all authors.

## Additional information

**Supplementary information** accompanies this paper at http://www.nature.com/scientificreports

**Competing financial interests:** The authors declare no competing financial interests.

**How to cite this article:** Tian, J. *et al.* Quantum and Classical Magnetoresistance in Ambipolar Topological Insulator Transistors with Gate-tunable Bulk and Surface Conduction. *Sci. Rep.* **4**, 4859; DOI:10.1038/srep04859 (2014).